Structural basis of fatty acid activation and transport by human FATP2

Ao Li[1,2,3,4#], Junhui Shi[1,3,4#], Xiaoyan Xu[1,5], Yu Yang[1,3,4], Shan Feng[1,5] & Dan Ma[1,3,4]

[1]State Key Laboratory of Gene Expression, Key Laboratory of Structural Biology of Zhejiang Province, School of Life Sciences, Westlake University, Hangzhou, Zhejiang, China.

[2] College of Agriculture and Biotechnology, Lishui University, Lishui, Zhejiang, China.

[3]Westlake Laboratory of Life Sciences and Biomedicine, Hangzhou, Zhejiang, China.

[4]Institute of Biology, Westlake Institute for Advanced Study, Hangzhou, Zhejiang, China.

[5]Mass Spectrometry Core Facility, The Biomedical Research Core Facility, Center for Research Equipment and Facilities, Westlake University, Hangzhou, Zhejiang, China.

These authors contributed equally: Ao Li and Junhui Shi

email: madan@westlake.edu.cn

Abstract

Fatty acid transport proteins (FATPs) are responsible for efficient uptake of fatty acids (FAs), essential biomolecules that play critical roles in development and growth. However, the lack of three-dimensional structures of FATPs has hindered our understanding of their mechanisms. Here, we report two cryo-EM structures of human FATP2a: wild-type (WT) FATP2a in intermediate state at 2.93 Å and a catalytic mutant of FATP2a in pre-catalytic state at 2.76 Å. In the two structures, both the oleoyl-AMP intermediate and ATP occupy the same central pocket with the acyl group of oleoyl-AMP pointing upwards and placed in a hydrophobic tunnel while the phosphate groups of ATP pointing downwards and interacting with a central loop. The structures also reveal that FAs from the membrane must undergo a two-step translocation to access the catalytic center. The binding of a new FA before the completion of

a working cycle may be crucial to ensure the catalytic and transport efficiency. Furthermore, we demonstrate that FATP2a transport FAs, strictly dependent on the activation of FAs through the acyl-CoA synthetase activity. Our findings provide important insights into the working mechanism of FATPs and offer a structural basis for the development of inhibitors targeting FATPs to treat related diseases.

Introduction

Fatty acids (FAs) play important roles in development and growth, primarily through their involvement in membrane biogenesis, energy metabolism, and cell signaling[1-4]. FAs can be classified according to their aliphatic chain length into short-chain (2–6 carbon atoms), medium-chain (8–12 carbon atoms), long-chain (14–18 carbon atoms), and very-long-chain (20–26 carbon atoms) FAs. In the circulation and tissues of mammals, FAs predominantly bear long and very long chains[5]. FAs are indispensable for numerous biological processes, including ATP generation via β-oxidation, the synthesis of structural lipids such as phospholipids and sphingolipids, and the synthesis of signaling molecules like eicosanoid[1-4,6]. Typically, FA molecules are activated by linking to Coenzyme A (CoA) to form acyl-CoA, a necessary intermediate for FA elongation, β-oxidation, phospholipid generation, and the synthesis of neutral lipids such as triacylglycerol (TAG)[7]. Furthermore, fatty acids may directly or indirectly interact with membranes, ion channels, transporters, hormone receptors, and enzymes, influencing various cellular functions[8].

Fatty acid transport proteins (FATPs) constitute a family of conserved membrane-bound proteins that facilitate the transport of long-chain fatty acids (LCFAs) and very-long-chain fatty acids (VLCFAs), which are limited in passive diffusion[9-11]. FA transport activity and ATP-dependent acyl-CoA synthetase activity for FA activation have been demonstrated in FATPs[12-18]. Six members of FATPs (FATP1-6) in humans exhibit distinct patterns in tissue distribution, expression, and subcellular localization, and are crucial for fatty acid uptake and utilization, as well as lipid homeostasis in corresponding tissues and cells[19]. Fatty acid uptake and metabolism are essential for cellular metabolic networks, particularly lipid metabolism, and an

imbalance in lipid flux can remodel or impair cell metabolism, leading to a variety of human diseases, including cancers and heart failure[20-24]. FATPs are important drug targets for the treatment of related diseases. Despite their importance, three-dimensional structures of these FA transport proteins are lacking, hindering a deeper understanding of their working mechanisms.

Here, we report two cryo-EM structures of human FATP2a at 2.93 Å and 2.76 Å resolutions, representing an intermediate state and a pre-catalytic state during FA activation and transport, respectively. Our results provide structural basis for understanding the mechanisms of acyl-CoA generation and FA transport by FATPs.

Results

Overall structure of FATP2 in intermediate state

FATP2 bears both acyl-CoA synthetase activity and fatty acid transport activity[12-18] (Fig. 1a and Supplementary Fig. 1a). To elucidate the working mechanism of FATP2 and understand the relationship between the two functions, we performed structural studies and biochemical analysis towards FATP2.

FATP2 has two natural splicing variants, the canonical splicing form of FATP2a that contains 620 amino acids and the alternative splicing form of FATP2b that contains 567 amino acids. In this study, full-length human FATP2a was recombinantly expressed in Expi293F cells and purified into homogeneity. Since AMP is one of the final products during FATP2-mediated acyl-CoA synthesis or fatty acid activation (Fig. 1a and Supplementary Fig. 1a), AMP production was measured by HPLC to represent the acyl-CoA synthetase activity. Wild-type (WT) FATP2a was reconstituted into peptidisc[25] to eliminate the inhibitory effects of detergents during enzymatic assay. FATP2a was found to catalyze AMP generation in a pH dependent manner showing no detectable activity at pH 4 and the highest activity at around pH 9.0 (Supplementary Fig. 1b). The accumulation of AMP was measured at pH 7.4 and the 2-minute time point within the linear range of substrate accumulation (Supplementary Fig. 1c), which

allowed the calculation of transport rate and the determination of Km values towards ATP and CoA as 402.20 μM and 75.59 μM, respectively (Supplementary Fig. 1d).

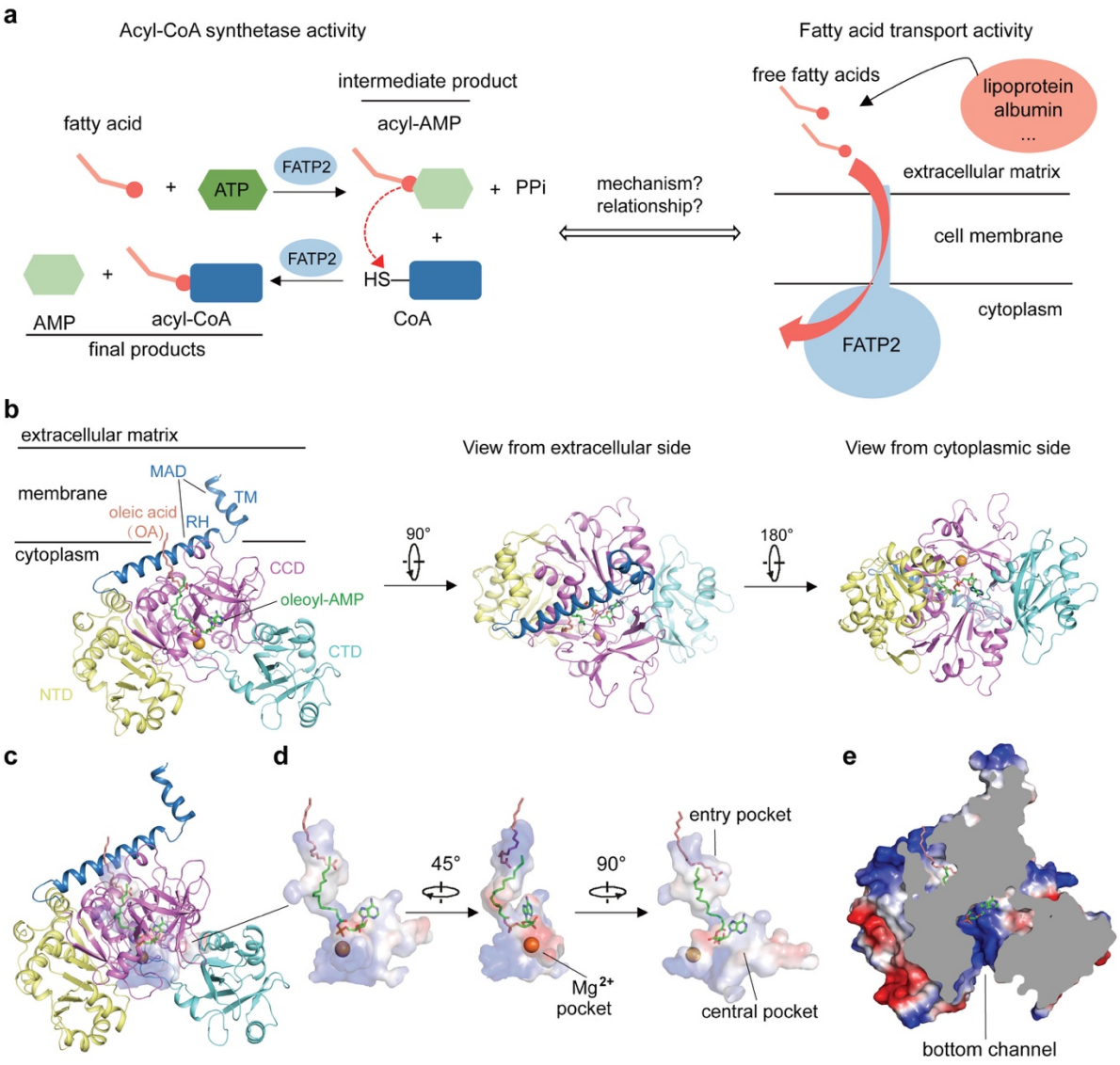

Figure 1. Cryo-EM structure of FATP2 in the intermediate state. a, An illustration of the acyl-CoA synthetase and fatty acid transport activities of FATP2. **b,** Overall structure of FATP2a. The membrane association domain (MAD), cytosolic N-terminal domain (NTD), core catalytic domain (CCD), C-terminal domain (CTD), oleic acid, oleoyl-AMP and Mg^{2+} are colored blue, yellow, violate, cyan, salmon, green and orange, respectively. **c,** The inner spaces for accommodation of oleic acid, oleoyl-AMP and Mg^{2+} in the FATP2 structure. Electrostatic surface was generated with only the culled cavities and pockets shown at 60% transparency. **d,** Different views of the continuous inner spaces with the entry pocket for oleic acid, central pocket for oleoyl-AMP and the binding pocket for Mg^{2+} indicated. **e,** A cut-away surface of the FATP2 structure. The large bottom channel is indicated.

WT FATP2a and a catalytic mutant (K572A) were reconstituted into nanodiscs (Supplementary Fig. 1e, f) for cryo-EM analysis. FATP2a and FATP2b variants were purified for validation of structural findings in this manuscript, and all purified proteins exhibited similar behavior (Supplementary Fig. 1f, g). Following data acquisition and processing, cryo-EM maps of WT and the catalytic mutant were obtained at 2.93 Å and 2.76 Å, enabling the building of structural models that represent an intermediate state and a pre-catalytic state, respectively (Supplementary Figs. 2-4 and Supplementary Table 1).

In the cryo-EM structure of FATP2a in the intermediate state, we observed that FATP2a is bound to an oleic acid, an oleoyl-AMP, the intermediate product during acyl-CoA synthesis, and a magnesium ion (Mg^{2+}) coordinated below the oleoyl-AMP (Fig. 1b and Supplementary Fig. 5a), with the bound ligands and ion confirmed by mass spectrometry analysis (Supplementary Fig. 5b-f). Quadrupole time-of-flight mass spectrometry (Q-TOF MS) results suggested that both oleic acid (C18:1) and palmitic acid (C16:0) were obviously enriched in the protein sample (Supplementary Fig. 5b), however the oleic acid with longer length fitted better into the corresponding density (Supplementary Fig. 5a). We speculate that palmitic acid may be randomly associated with FATP2a in other regions. The identity of the bound ion was confirmed to be Mg^{2+} by inductively coupled plasma mass spectrometry (ICP-MS) (Supplementary Fig. 5c). Q-TOF MS results also demonstrated the existence of a molecule in the FAPT2 sample harboring the same m/z ratio with oleoyl-AMP (Supplementary Fig. 5d, e). We further performed Q-TOF MS analysis of FATP2 samples with or without NaOH treatment and determined the change in abundance of the possible oleoyl-AMP, oleic acid and AMP. The results suggested that after NaOH-mediated hydrolysis, the peak possible for oleoyl-AMP disappeared, while the abundance of free oleic acid and AMP were dramatically increased (Supplementary Fig. 5f), confirming the identity of oleoyl-AMP.

FATP2a is composed of four domains: the membrane association domain (MAD), the cytosolic N-terminal domain (NTD), the core catalytic domain (CCD), and the C-terminal domain (CTD) (Fig. 1b). The cytosolic regions of FATP2a form an arch-like structure, with the NTD and CTD situated on opposite sides of the CCD. The MAD comprises an N-terminal

transmembrane helix (TM), of which only the C-half is modeled based on the density, and a subsequent reclining helix (RH) attached to the membrane. MAD serves as an anchor, fixing FATP2a to the membrane. The N-half of RH interacts with the membrane by inserting hydrophobic residues, while the C-half of the RH may be attracted to the membrane through electrostatic interactions between the negatively charged phosphate groups of lipids and positively charged residues in the RH (Supplementary Fig. 6a). Both the NTD and CTD are similarly arranged into β-α-β-α structures (Supplementary Fig. 6b, c). The CCD domain exhibits a saddle-shaped structure, with two subdomains arranged side by side, accommodating the MAD-RH in the middle groove (Supplementary Fig. 6d).

The oleic acid is bound at the interface between the membrane and FATP2a (Fig. 1b, c). The half of the FA on the hydrophobic tail side (tail-half) interacts with the membrane and RH, while the half on the polar head side (head-half) is inserted into a pocket on the top of CCD, referred to as the entry pocket (Fig. 1d). The oleoyl-AMP is located below the oleic acid in a large central pocket with the acyl group placed in a tunnel connecting the entry pocket and the central pocket (Fig. 1d). The cofactor Mg^{2+} is coordinated below the oleoyl-AMP in CCD (Fig. 1d), indicating that the reaction center for acyl-CoA synthetase activity is likely situated nearby. The carboxyl group of the oleic acid is about 18 Å away from the Mg^{2+} and thus distant from the reaction center, and therefore we named the FA which has not reach the catalytic center as a pre-entry FA. We speculate that the FA substrate must be translocated to gain access to the reaction center for catalysis. Additionally, below the oleoyl-AMP, a large vertical channel faces the cytoplasm (Fig. 1e and Supplementary Fig. 6e), which may allow the passage of other substrates and products.

The binding site of pre-entry FA substrate

The pre-entry oleic acid at the entry pocket has a crescent shape and wraps around RH in FATP2a, with the tail side inserted into the nanodisc, interacting both with RH and lipids in the nanodisc (Fig. 2a, b). It may represent the interaction mode between FAs and native membrane environment when FAs are initially captured and mounted onto FATP2. The head-

half of the oleic acid binds into the hydrophobic entry pocket formed by hydrophobic residues from both RH and CCD at the interface between the nanodisc and the cytosolic portion of FATP2a (Figs. 1d, 2b). The hydrophobic tail of the oleic acid interacts with Tyr32, Phe33, Val36, Ala37, and Val39 in RH, and Tyr244, Leu248, Val251, Ile391, Ile392, and Leu432 in CCD. Additionally, a hydrogen bond is formed between the carboxyl group of the FA and the hydroxyl group of Tyr32 in RH, which may further stabilize the binding.

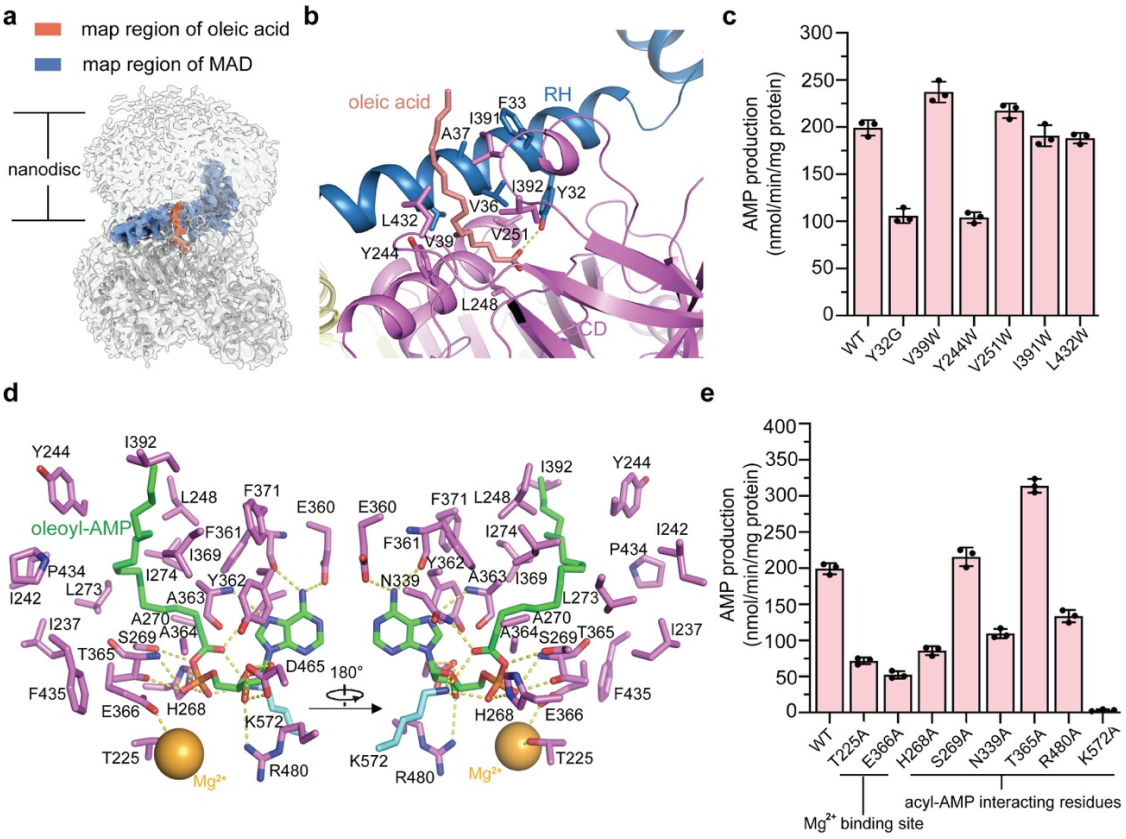

Figure 2. The binding sites of ligands and ion in the structure of FATP2 in the intermediate state. **a,** The oleic acid binding in the cryo-EM map. Map regions of the FA and MAD are highlighted and map region of nanodisc is indicated. **b,** The binding details between the pre-entry oleic acid and FATP2a. **c,** The acyl-CoA synthetase activity of pre-entry FA binding site mutants compared to that of WT FATP2a. AMP production was measured to represent the enzymatic activity. **d,** Interaction details at the oleoyl-AMP and Mg^{2+} binding sites. **e,** AMP generation by WT FATP2a and mutants carrying mutations at Mg^{2+} and oleoyl-AMP binding sites. All enzymatic assay data are shown as mean ± SD, n = 3 biological replicates. Source data are provided as a Source Data file.

To validate the importance of the interactions between oleic acid and FATP2 at the entry pocket, we generated FATP2a mutants with alterations in the FA entry pocket and examined their effects on enzymatic activity. We aimed to disrupt the polar interaction mediated by Tyr32 or reduce the pocket volume by mutating entry-pocket-forming residues that are closed to and pointing towards the pre-entry FA into an amino acid with bulky side chain. Compared to WT FATP2a, AMP production decreased by approximately 50% for the Y32G mutant, which may disrupt the interaction between the polar head of FA substrate and FATP2a, and for the Y244W mutant, which may reduce the pocket volume and restrict the entry of FAs (Fig. 2c). These findings suggest that the initial binding of the FA substrate at the entry pocket is crucial for the acyl-CoA synthetase activity of FATP2.

The binding sites of oleoyl-AMP and Mg^{2+}

In the structure in intermediate state, the intermediate product oleoyl-AMP is primarily bound to CCD (Figs. 1b, 2d) in the central pocket, with the acyl group positioned in the connection tunnel between the FA entry pocket and the central pocket (Fig. 1d). Extensive interactions are generated between the oleoyl-AMP and FATP2a, and the Mg^{2+} is bound below the oleoyl-AMP (Fig. 2d), closed to the phosphate group of oleoyl-AMP. The oleoyl-AMP forms hydrogen bonds with side chains of His268, Ser269, Asn339, Glu360, Thr365, Asp465, Arg480 and Lys572, as well as with the main chains of Phe361, Ala363 and Thr365. The phosphate group of the AMP portion engages in electrostatic interactions with Arg480 and Lys572, with Lys572 in CTD being the only residue from a different domain besides CCD. The hydrophobic acyl group of oleoyl-AMP is placed in the tunnel connecting the FA entry pocket and the central pocket. This tunnel is primarily composed of hydrophobic residues, including Ile237, Ile242, Tyr244, Leu248, Ala270, Leu273, Ile274, Phe361, Tyr362, Ala363, Ala364, Ile369, Phe371, Ile392, Pro434 and Phe435. The Mg^{2+} bound below is coordinated by Thr225 and Glu366, which is further stabilized by the negatively charged phosphate group of oleoyl-AMP.

To examine the importance of the residues at the binding sites of Mg^{2+} and oleoyl-AMP, we introduced mutations and compared corresponding AMP production of the mutants to that of WT FATP2a (Fig. 2e). The AMP production of both Mg^{2+} binding site mutants, carrying the T225A or E366A mutations, were significantly decreased, with the E366A mutant exhibiting a reduction of more than 70% (Fig. 2e). We also measured the enzymatic activity of FATP2a variants bearing mutations in residues involved in polar interactions with the oleoyl-AMP. The results suggested that the mutants carrying H268A, N339A, R480A and K572A mutations exhibited reduced enzymatic activity, with almost no acyl-CoA synthetase activity could be detected for the K572A mutant (Fig. 2e). Besides generating electrostatic interactions with the phosphate group in oleoyl-AMP, both His268 and Lys572 form hydrogen bonds with the same hydroxyl oxygen of the phosphate group, while Lys572 also forms additional hydrogen bonds with oxygens from the ribose ring and the carbonyl group of the acyl moiety (Fig. 2d). It seems that Lys572 is important for the binding of intermediate product acyl-AMP and is essential for the enzymatic activity of FATP2a. Surprisingly, the mutant carrying the T365A mutation increased FATP2a-mediated AMP production by more than 50% (Fig. 2e). We speculate that the mutation of Thr365 might facilitate the access of the acceptor group for the acyl moiety in CoA to the ester linkage and/or enhance the rate of product release during the reaction.

The FATP2 structure in pre-catalytic state

We stabilized ATP binding of FATP2a with the K572A mutant which is unable to catalyze ATP hydrolysis and thus obtained the cryo-EM structure of FATP2 in pre-catalytic state (Fig. 3a and Supplementary Fig. 7). In this structure, FAPT2a is bound with two oleic acids, one is pre-entry (OA1) and the other one (OA2) is moved downwards into the connection tunnel between the entry pocket and central pocket, with the tail end swung into a side tunnel and the carboxyl group placed near to the catalytic center (Fig. 3b). This structural finding is consistent with our previous speculation that FA substrates need to be translocated downwards to gain access to the catalytic center.

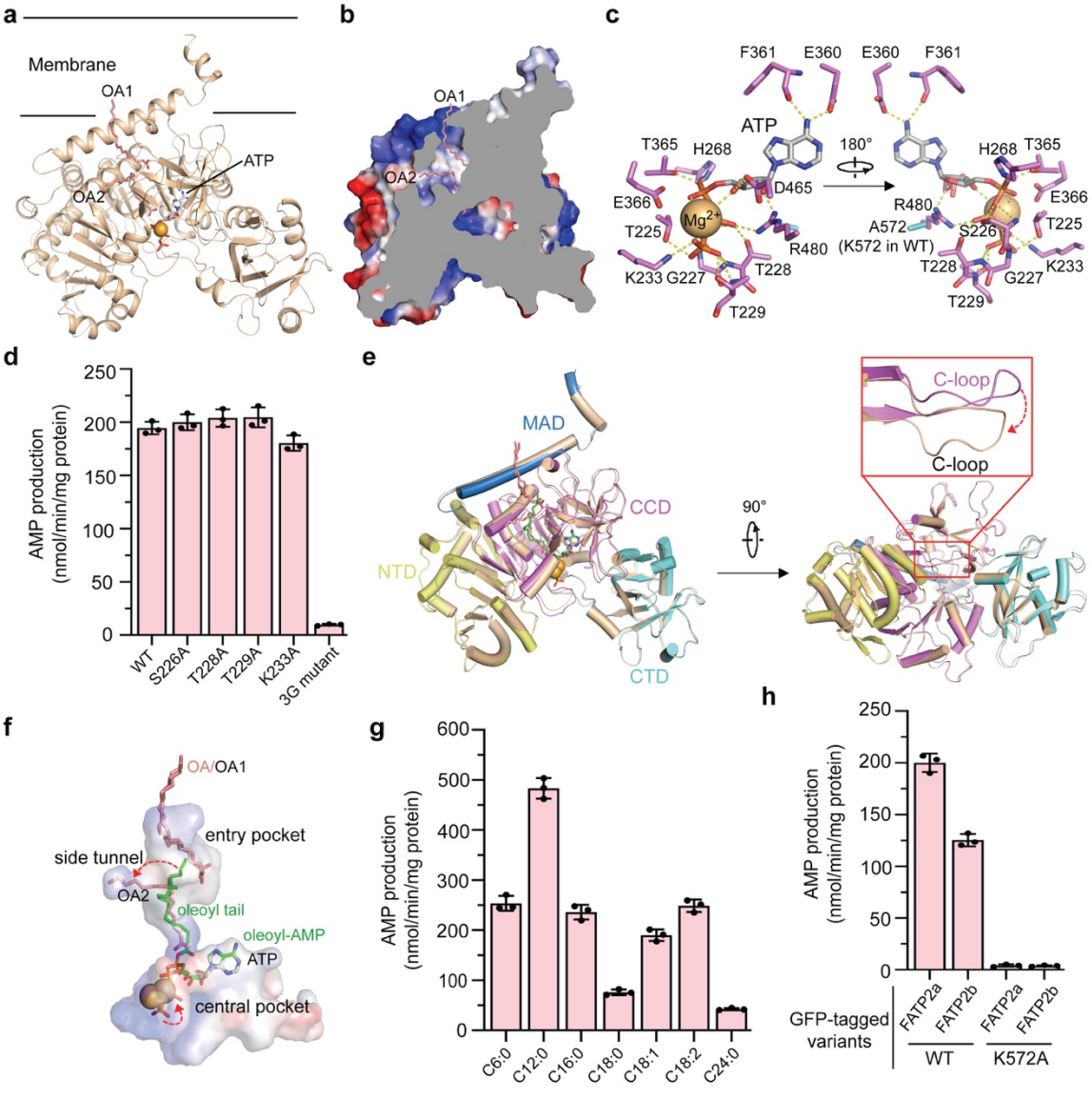

Figure 3. The structure of FATP2 in the pre-catalytic state and biochemical validations. a, Overall structure of FATP2a in pre-catalytic state. FATP2a, oleic acid (OA), ATP and Mg^{2+} are colored wheat, salmon, grey and orange, respectively. **b,** A cut-away surface of the FATP2a structure with the two oleic acids indicated. **c,** Interaction details between FATP2a and ATP. The alanine substitution at position 572 is also indicated. **d,** AMP generation by WT FATP2a and mutants carrying mutations at residues specifically involved in ATP binding. **e,** Structural alignment between the FATP2 structures in pre-catalytic state and intermediate state. **f,** Comparison of the binding of ligands and Mg^{2+} in the pockets of the two structures. **g,** AMP generation by FATP2a using different FA substrates. During enzymatic assay, cyclodextrin was used to increase the solubility of corresponding FAs. **h,** Comparison of the enzymatic activities of FATP2a and FATP2b. GFP was fused on the N-terminal to facilitate the expression of FATP2b. The K572A mutants were used as negative control. All enzymatic assay data are shown as mean ± SD, n = 3 biological replicates. Source data are provided as a Source Data file.

ATP is bound into the central pocket with the phosphate groups oriented downwards. Majority of the residues interacting with ATP are also involved in acyl-AMP binding, including Lys572, which was mutated to alanine in the mutant. However, the phosphate groups in ATP generate new hydrogen-bonding interactions with a central loop (C-loop) formed by Thr225, Ser226, G227, T228 and T229, which are further stabilized by electrostatic interactions with Lys233 and the Mg^{2+} (Fig. 3c). A triple mutant of S226/T228/T229G reduced the enzymatic activity of FATP2a by more than 90%, demonstrating the importance of the C-loop (Fig. 3d).

Structural alignment between FATP2 in both structures suggests that the protein structures are almost identical, except that the C-loop flips due to binding to the phosphate groups of ATP (Fig. 3e). Comparisons of the ligands binding in the pockets suggested that the pre-entry oleic acids as well as the ring-containing portions in ATP and oleoyl-AMP bind similarly in the two structures, while an anticlockwise rotation happens between the tail of the downwards translocated oleic acid and acyl moiety of the oleoyl-AMP (Fig. 3f). Actually, in the cryo-EM map of the FATP2 structure in intermediate state, we also noticed some densities in the same side tunnel that accommodating the OA2 tail in the map of mutant, indicating that the tail of the oleoyl-AMP might also be alternatively inserted into the side tunnel. Besides above differences, the Mg^{2+} is also moved towards the central pocket due to the attraction by the phosphate groups of ATP (Fig. 3c, f).

To investigate the preferences of FATP2 towards different FAs, we examined the AMP producing efficiency of FATP2a using FA substrates with different lengths and degree of saturation. We performed enzymatic assay using C6:0, C12:0, C16:0, C18:0, C18:1, C18:2 and C24:0 FAs, among which C8:0 and C12:0 FAs were totally dissolved while the rest had low solubility and used as saturated solution in the presence of cyclodextrin. It turned out that when C12:0 FA was used as substrate, FAPT2a exhibited high enzymatic activity; when C6:0, C16:0, C18:1 (oleic acid), C18:2 FAs were used, FAPT2a exhibited mediate level of enzymatic activity; whereas when C18:0 and C24:0 FAs were used, FATP2a showed lower activity (Fig. 3g). These results indicate that FATP2 seems to most prefer FA substrate with medium chain length for catalysis. The results of C18 substrates suggested that unsaturated form might be

more favorable for catalysis by FATP2, however it is also possibly due to the relatively higher solubility of unsaturated FAs. Nonetheless, the substrate choices in physiological conditions may be heavily dependent on the abundance of FAs.

Besides FATP2a, there is an alternative splicing variant of FAPT2 named as FATP2b. Sequence alignment result suggests that FATP2b lacks the residues from 230 to 282 in FATP2a, involving Ile237, Ile242, Tyr244, Leu248, Ala270, Leu273, Ile274 that form the connection tunnel and His268 and Ser269 that form polar interactions with the phosphate groups of ATP and acyl-AMP (Fig. 2d, 3c and Supplementary Fig. 8a). The residues 230-282 are found to locate in the center of FATP2a and contribute to the formation of the connection tunnel and partial of the central pocket in the cryo-EM structure of FATP2a (Supplementary Fig. 8b). Our in vitro assay results indicate that FATP2b also has acyl-CoA synthetase activity, however with approximate 1/3 decrease in AMP production compared to that of FATP2a (Fig. 3h). Interestingly, the results suggest that FATP2b exhibits less decrease in AMP production compared to the FATP2a-H268A mutant (Fig. 2e, 3h). These results indicate that a structural rearrangement in FATP2b may occur to compensate the loss of polar interaction mediated by His268 as well as the forming-residues of the hydrophobic connection tunnel.

Fatty acid transport by FATP2

To examine FA transport activity of FATP2, we performed a proteoliposome-based transport assay (Fig. 4a). C1-BODIPY-C12, a fluorescence-labeled fatty acid derivative widely used to monitor fatty acid uptake[12,26,27], was incorporated into the lipid bilayer during liposome preparation and serves as the FA substrates for FATP2. Additional substrates and co-factors were added to the outside assay buffer to initiate FA transport towards the external environment, and bovine serum albumin (BSA) was supplemented outside for binding with the hydrophobic acyl tail of the exported FA substrates to increase their solubility. The resulting external fluorescence was recorded after the removal of the liposomes.

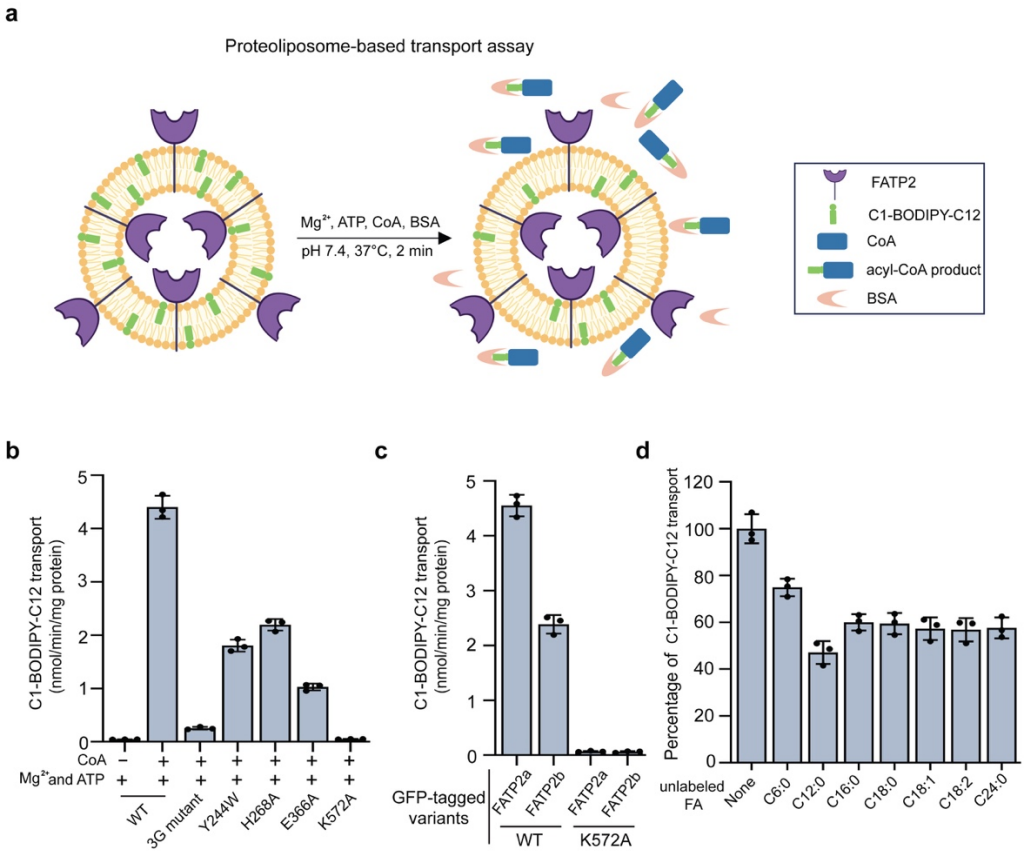

Figure 4. Substrate transport by FATP2. a, A proteoliposome-based assay for the measurement of FA transport. The fluorescence-labeled FA derivative C1-BODIPY-C12 was used as the FA substrate and incorporated into the proteoliposomes. Mg^{2+}, ATP and CoA were supplemented into the external buffer at pH 7.4 and lasted for 2 min at 37°C for reaction. The C1-BODIPY-C12 molecules in the lipid bilayer were transported by the outward-oriented FATP2 towards external environment. Transport was terminated by adding buffer at pH 4.5 and liposomes were removed through centrifugation before fluorescence of supernatant for FATP2 variants were recorded. The liposome part in the figure was created in BioRender. Ma, D. (2026) https://BioRender.com/x2jkypf. **b,** Substrate transport activity of FATP2a variants with or without the presence of CoA. **c,** Comparison of substrate transport by FATP2a and FATP2b. The K572A mutants were used as negative control. **d,** Substrate preference of FATP2a for transport. Competition transport assay was performed by incorporating unlabeled FAs with different length and unsaturation degree to examine the inhibitory effects on C1-BODIPY-C12 transport. The reading of supernatant corresponding to proteoliposomes without the supplementation of unlabeled FA was taken as 100%. For all transport assay, data are shown as mean ± SD, n = 3 biological replicates. Source data are provided as a Source Data file.

Transport assay results suggested that WT FATP2a efficiently transported C1-BODIPY-C12 towards outside when Mg^{2+}, ATP, and CoA were supplemented; however, almost no substrate transport was detected in the absence of CoA (Fig. 4b). We also evaluated substrate transport by some representative FATP2a mutants which exhibited reduced enzymatic activity to different levels (Figs. 2c, e and 3d), and the results showed that the transport activity of the mutants were decreased follow a similar trend, with mutation of the catalytically essential Lys572 to alanine abolished substrate transport (Fig. 4b). The transport rate was much lower compared to the AMP converting rate probably mainly because the concentration of C1-BODIPY-C12 (20 μM) in transport assay was much lower than the concentration of FAs (500 μM) during enzymatic assay, and the differences may also be resulted from the nature of the substrate derivative and the membrane-like environment during transport assay. Transport activity of FATP2b was also examined, and it turned out that substrate transport by FATP2b was about half of that of FATP2a (Fig. 4c). These findings demonstrate that both forms of FATP2 have fatty acid transport activity, and FATP2-mediated FA transport is stringently dependent on FA activation through the acyl-CoA synthetase activity.

To further learn FA preference for transport, we performed competition transport assay by incorporating unlabeled FAs together with C1-BODIPY-C12 during liposome preparation at molar ratio of 3:1. There were no solubility problems since FAs were first solubilized by organic solvent during liposome preparation. C6:0, C12:0, C16:0, C18:0, C18:1, C18:2 and C24:0 FAs were used as the competition substrates during transport assay. We found that C12:0 FA had greatest inhibition effects towards C1-BODIPY-C12 transport compared to other FAs, suggesting that the C12:0 FA is the most preferred substrate among the tested FAs (Fig. 4d), consistent with the substrate preference for enzymatic assay. No significant differences were found between the C18 FAs with different saturation degree (Fig. 4d), suggesting that saturation degree of FAs may not be a key determinant for FA transport by FATP2.

Discussion

Based on our structural findings and biochemical analysis, we propose a working model for FATP2 during one FA transport cycle dependent on FA activation (Fig. 5).

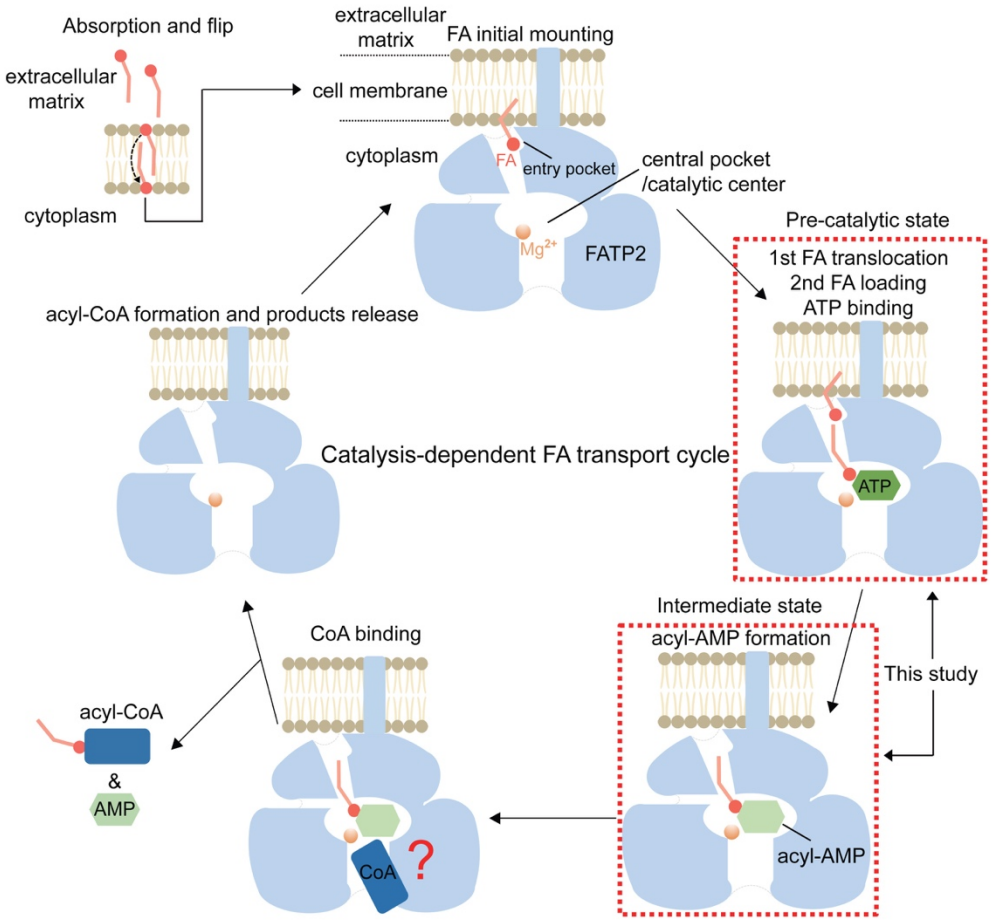

Figure 5. A working model for FATP2-mediated FA transport. FA absorbed by membrane is first mounted to FATP2 at the entry pocket, followed by translocation to the central pocket and gain access to the catalytic center for the generation of acyl-AMP in the presence of ATP. CoA binds to FATP2 with its thiol group reaching to the reaction center for the acceptance of the acyl-group from acyl-AMP. The final products acyl-CoA and AMP will be released into cytoplasm. A new FA substrate may be extracted from the membrane and mounted into the entry pocket as long as it is empty.

A FA substrate absorbed by membrane from the extracellular matrix is first captured by FATP2 followed by initial mounting at the entry pocket, and the FA substrate will be subsequently translocated to the catalytic center, where Mg^{2+} and ATP are bound to generate acyl-AMP. CoA will bind to FATP2, though the binding details are unclear due to the difficulties in obtaining the atomic 3D structure, with its thiol group gaining access to the reaction center

to accept the acyl group from acyl-AMP. The final products AMP and acyl-CoA will be generated after the transfer of acyl group from acyl-AMP to CoA and released to the cytoplasmic side. Fatty acids are transported into the cytoplasm by FATP2 in the form of acyl-CoA. During the catalysis-dependent FA transport process, substrates and products may be exchanged through the bottom, cytoplasm-facing channel, which is ideal in size and location. A new FA substrate from the membrane can bind to the entry pocket if there is a vacancy, regardless of the stage of the reactions. Catalysis-coupled FA transport cycles mediated by FATP2 may provide the driving force for the incorporation of FAs into the membrane, which may further provide substrates for FATP2, and thus enhance FA uptake.

Sequence alignment results indicate that it is conserved among all six human FATPs (Supplementary Fig. 9) and among FATP2s across species (Supplementary Fig. 10). Residues in the reaction center involved in binding with Mg^{2+} and the AMP portion of acyl-AMP or ATP, as well as those forming the bottom channel possible for substrate/product passage, are highly conserved. Interestingly, residues involved in binding with the FA substrate and the acyl group of acyl-AMP, although similar in hydrophobic properties, are less conserved. This may result in variable preferences for FA substrates among FATPs. Structural comparisons between our cryo-EM structure of FATP2 and AlphaFold-predicted structures of other human FATPs suggest that all six FATPs are structurally conserved in the cytosolic regions (Supplementary Fig. 11a-c). Therefore, other FATPs may share similar mechanisms for FA activation and transport.

FATPs belong to the acyl-CoA synthetase (ACS) gene family, a protein family with conserved motifs identified via sequence alignment and biochemical analyses across the family members[28]. The key residues in the reaction center of FATP2 involved in binding with Mg^{2+}, the AMP portion of acyl-AMP and ATP can be found in these conserved motifs. For instance, our structural and biochemical analyses suggested that the C-loop region is important for ATP binding and thus the enzymatic activity, consistent with previous postulations that this region may be the ATP-binding motif[28-30]. Meanwhile, extensive interactions between this loop region and ATP have also been observed in the crystal structure

of another ACS family member, human ACSM2A in complex with ATP, further supporting our structural finding and conclusion regarding FATP2[31]. We also demonstrated that Lys572 is an essential amino acid at the catalytic site, the mutation of which abolished the FATP2a activities in fatty acids activation and transport. Similarly, this lysine residue is present in a conserved motif, and it's reported that the mutation of the conserved lysine also led to the loss of catalytic activity in other acyl-CoA synthetases[32,33]. Furthermore, our study identified Thr225 and Glu366 as Mg^{2+}-coordinating residues, both of which are in another conserved motif. Notably, the homologous residues in ttLC-FACS (a bacterial ACS family member) were also found to interact with Mg^{2+} in its crystal structures[34]. These results indicate the conservation of the catalytic mechanism among ACSs.

Accurate 3D structural information of FATPs is important for drug development. In a previous study, an apo structural model of the intracellular part (residues 54-583) of human FATP2 was generated through homology modeling and subsequently used for *in silico* screening of FATP2 inhibitors[35]. However, due to lacking the structural information of membrane association region and ligands binding details, the molecular mechanism of FATP2-mediated FA transport was not elucidated, and the targetable sites for inhibitors could not be precisely identified. Currently, the most effective and commonly used FATP2 inhibitors (e.g., lipofermata, grassofermata, and CB-6) remain inadequate for clinical trials due to their prohibitively high IC_{50} values and lack of pharmacokinetic data[36,37]. We performed AlphaFold3 predictions of FATP2 in complex with lipofermata, grassofermata and CB-6, and the results suggest that these inhibitors may bind at the lower FA binding site (Supplementary Fig. 11d-f). Our structural and biochemical analysis suggest that the entrance pocket for FA loading, the central pocket for ATP/acyl-AMP binding, the catalytic essential lysine residue as well as the central loop for ATP binding could also be potential sites for drug discovery to inhibit FAPT2 activity through abolishing the catalytic activity of FATP2 or disrupting its binding to ligands. The findings in this study may also benefit drug discovery towards other FATPs.

Taken together, our studies reveal structural features of FATP2 and its binding modes with the substrates of FAs and ATP as well as the acyl-AMP intermediate product, facilitating

the identification of a conserved catalytic site and other important structural elements. These findings offer crucial insights into the activation and transport mechanisms of FAs by FATP2, which also enhance our understanding of the molecular mechanisms of other FATPs and ACSs. This study also provides a structural foundation for the development of inhibitors targeting FATP-mediated FA activation and transport, with potential applications in the treatment of related human diseases, including cancers.

Methods

Protein expression and purification

Human FATP2 (UniProt ID: O14975) variants were cloned into pCAG vector with an N-terminal FLAG-tag (WT FATP2a and related mutants) or an N-terminal FLAG-GFP-tag (WT FATP2a and FATP2b). Plasmids were transiently transfected into Expi293F cells at density of 2.0×10^6 cells/ml and cultured in SMM 293-TII medium (Sino Biological) at 37 °C under 5% CO_2. After 60 h, cells were harvested and resuspended in the buffer containing 25 mM HEPES pH 7.4, 150 mM NaCl, 5 μg/ml aprotinin, 1 μg/ml pepstatin, 5 μg/ml leupeptin and 1 mM PMSF. Cell membrane was solubilized with 1% (w/v) n-dodecyl-β-D-maltoside (DDM, Anatrace) at 4 °C for 2 h. After centrifugation at 25,000 g for 1 h, the supernatant was loaded onto anti-FLAG resin (GenScript). Then the resin was washed with buffer containing 25 mM HEPES pH 7.4, 150 mM NaCl, and 0.03% (w/v) DDM. For Cryo-EM sample preparation, FATP2a was eluted with wash buffer supplemented with FLAG peptide at 0.2 mg/ml concentration. For preparation of proteoliposomes, proteins were eluted with buffer containing 1% (w/v) n-octyl-β-D-glucopyranoside (β-OG, Anatrace) (for N-FLAG-tagged WT FATP2a and K572A mutant) or 0.03% (w/v) DDM (for N-FLAG-GFP-tagged WT FATP2a and FATP2b).

The membrane scaffold protein MSP1D1 bearing N-terminal His-tag for nanodisc reconstitution was expressed in *E. coli* BL21(DE3) cells. Cells were lysed by sonication in lysis buffer (20 mM sodium phosphate buffer, pH 7.4) supplemented with 1 mM PMSF and 1% Triton X-100. After centrifugation at 30,000 g for 30 min at 4 °C, the supernatant was loaded onto the nickel-affinity resin. The resin was washed with 40 mM Tris/HCl pH 8.0, 300 mM NaCl, 5 mM sodium cholate and 30 mM imidazole. Protein was eluted with elution buffer containing

10 mM Tris/HCl pH 7.4, 100 mM NaCl, 5 mM sodium cholate and 300 mM imidazole. The elution was concentrated and loaded onto a Superdex 200 Increase column for further purification. The MSP1D1-containing fractions were pooled for nanodisc reconstitution.

Reconstitution of FATP2a into lipid nanodiscs

1-palmitoyl-2-oleoyl-sn-glycero-3-phospho-(1'-rac)-choline (POPC, Avanti Polar Lipids) and 1-palmitoyl-2-oleoyl-sn-glycero-3-phospho-(1′-rac-glycerol) (sodium salt) (POPG, Avanti Polar Lipids) were solubilized in chloroform at 1:3 molar ratio. Above solution was dried under nitrogen gas and resuspended to 5.76 mg/ml (7.5 mM) with buffer containing 2.5 mM cholesteryl hemisuccinate tris salt (CHS, Anatrace) and 30 mM DDM. FATP2a, MSP1D1 and lipid mixture were mixed at a molar ratio of 1:5:60 with the supplementation of the FATP2 inhibitor lipofermata[36,37] at final concentration of 0.5 mM, and incubated at 4 °C for 30 min. Detergents were removed by incubation with Bio-beads SM2 (Bio-Rad) overnight at 4 °C. The protein-lipid mixture was loaded onto a size-exclusion column equilibrated with 25 mM HEPES pH 7.4, 150 mM NaCl. The purified nanodiscs were collected for cryo-EM sample preparation.

Cryo-EM sample preparation and data collection

The FATP2a reconstituted into nanodiscs at protein concentration of 9 mg/ml was used for cryo-EM sample preparation. 3 μl of protein sample was applied onto each grid followed by a 3.5 s blotting using Vitrobot Mark IV (ThermoFisher Scientific). After blotting, grids were rapidly immersed into pre-cooled liquid ethane and transferred to liquid nitrogen. Image acquisitions were performed on Titan Krios G4 (FEI) operating at 300 kV with a Selectris X imaging filter (Thermo Fisher Scientific) and Falcon 4i direct electron detector (Thermo Fisher Scientific). Data were collected in counted super-resolution mode at magnification of 215,000 x, physical pixel size of 0.57 Å. Movie stacks were automatically acquired using Thermo Scientific EPU (Thermo Fisher Scientific) with a 20 eV slit width and a defocus range from −0.9 to − 1.5 μm. The movies were stored as EER format which were exposed for 2.45 s with total dose of ~50 e^{-}/Å^2.

Cryo-EM data processing

The cryo-EM data processing workflows are illustrated in Supplementary Figs. 2, 3. Motion-correction and dose weighting were performed using Patch Motion Correction in cryoSPARC[38]. Contrast transfer function (CTF) parameters were estimated with Patch-CTF in cryoSPARC. Micrographs with CTF fitting resolution worse than 6 Å were excluded during manual curation. Initial particles were picked from few partial micrographs using blob picker in cryoSPARC and 2D averages were generated.

For dataset of the WT FATP2a, final particle picking was done by template picker using templates from those 2D results. 4313 k particles were extracted from 14265 micrographs with pixel size of 9.12 Å (box size 30 pixels), After one round of 2D classification, the good particles were re-extracted and re-centered with pixel size of 4.56 Å (box size 60 pixels) for the next 2D classification. Above process was continued until the particles were re-extracted with pixel size of 1.14 Å (box size 240 pixels). After 4 rounds of 2D classification to remove obvious junk, a total of 129 k particles were retained. This data set was then used for ab-initio reconstruction, with carefully tuning parameters including the number of classes, initial resolution, initial and final minibatch sizes using cryoSPARC. A resulting map with better features was generated from ab-initio reconstruction. After non-uniform (NU) refinement[39], a good reference at 4.27 Å resolution was generated for the next 3D classification.

Another 12952 micrographs were combined with above 14265 micrographs, from which a total of 7307 k particles were extracted with pixel size of 9.12 Å (box size 30 pixels). These particles were subjected to 4 rounds of 2D classification and 275 k particles with pixel size of 1.14 Å remained. The map at 4.27 Å resolution was used as a good reference for the hetero refinement of the 275 k particles. After hetero refinement and NU-refinement, a map with a resolution of 3.54 Å was reconstructed using 137 k particles. To further improve the resolution, seed-facilitated 3D classification[40] was performed. A dataset as the seed pool, containing 1929 k particles was re-extracted with pixel size of 0.57 Å (box size 480 pixels). The above 137 k particles were also re-extracted with pixel size of 0.57 Å (box size 480 pixels) and were used as seeds for seed-facilitated 3D classification. After 3 rounds of seed-facilitated 3D classification, 469 k particles were subjected to NU-refinement, which resulted in map with a

resolution of 3.13 Å. After hetero refinement, ab-initio reconstruction and NU-refinement, a final map at 2.93 Å resolution was reconstructed by 143 k particles.

For the dataset of FATP2-K572A mutant, 8426 k particles were extracted from 14759 micrographs with pixel size of 4.56 Å (box size 48 pixels), After one round of 2D classification, the good particles were re-extracted and re-centered with pixel size of 2.28 Å (box size 96 pixels) for the next 2D classification. Above process was continued until the particles were re-extracted with pixel size of 1.14 Å (box size 192 pixels). After 3 rounds of 2D classification to remove obvious junk, a total of 101 k particles were retained for 3D classification. A resulting map with better features was generated from ab-initio reconstruction, which was used to create templates for following processing.

Another 37515 micrographs were combined with above 14795 micrographs, from which a total of 19597 k particles were extracted with pixel size of 4.56 Å (box size 48 pixels). These particles were subjected to 4 rounds of 2D classification and 808 k particles with pixel size of 1.14 Å remained. This data set was then used for ab-initio reconstruction, with carefully tuning parameters including the number of classes, initial resolution, initial and final minibatch sizes using cryoSPARC. After ab-initio reconstruction and NU-refinement, a map with a resolution of 3.02 Å was reconstructed using 221 k particles. To further improve the resolution, the above 808 k particles was subjected to hetero refinement, and the good reference was also used for the classification. After additional ab-initio reconstruction, hetero refinement and NU-refinement, the dataset of FATP2-K572A mutant in ATP-bound state gave rise to a reconstruction at an average resolution of 2.76 Å.

Model building and refinement

The initial structure models for WT FATP2a and K572 mutant were generated by AlphaFold2[41] and AlphaFold3[42], respectively. The structures were docked into the density map and manually adjusted and re-built by COOT[43]. Model refinement was performed using phenix.real_space_refine in PHENIX[44]. For cross-validations, the model vs. map Fourier Shell Correlation (FSC) curves were generated in the Comprehensive Validation module in PHENIX. The structure was validated through examination of the Molprobity scores[45], and statistics of

the Ramachandran plots. Local resolutions were estimated using cyroSPARC local resolution estimation. Structural Figures were generated using PyMOL[46], UCSF Chimera[47] and ChimeraX[48].

LC–MS analysis of fatty acids contents

To extract the lipids and fatty acids contents, 100 µl of each protein samples (29.3 µM) was first reduced with 5 mM DTT at 35 ℃ for 30 min and further alkylated with 20 mM iodoacetamide at 25 ℃ for 30 min. Then the samples were digested with trypsin at an enzyme-to-protein ratio of 1:50 (w/w) at 37 ℃ overnight. Methanol (1.5 ml) was added to each digested protein sample and thoroughly mixed before the supplementation of 5 ml of MTBE for 1 h of incubation at room temperature. Phase separation was induced by adding 1.25 ml of MS-grade water followed by 10 min incubation at room temperature and then centrifugation at 1,000 g for 10 min. The upper (organic) phase was collected. The lower phase was reextracted with 2 ml of the solvent mixture at MTBE: methanol: water ratio of 10:3:2.5 (v/v/v) and the resulting upper phase was combined with the previous upper phase and dried in a vacuum centrifuge.

Fatty acid content was analyzed using an LC-MS system comprising an Agilent 1290 Infinity II UHPLC system tandem with an Agilent 6545 Q-TOF/MS (Agilent). Extracted lipids/fatty acids were dissolved in 200 µl of dichloromethane/methanol (3:1, v/v) for storage. Chromatographic separation was achieved on an ACQUITY UPLC BEH C18 column (100 mm × 2.1 mm, 1.7 µm) with the mobile phase consisting of 10 mM ammonium acetate, 0.2 mM ammonium fluoride in 9:1 water/methanol as solvent A and 10 mM ammonium acetate, 0.2 mM ammonium fluoride in 2:3:5 acetonitrile/methanol/isopropanol as solvent B. MS data were acquired using electrospray ionization in negative ion mode over 40-1700 m/z. The additional MS parameters were set as follows: sheath gas temperature at 300 °C, sheath gas flow at 11 l/min, Nebulizer pressure at 35 psi, drying gas flow at 8 l/min, VCap at 3500 V, gas temperature at 275 °C, fragmentor voltage at 150 V, and skimmer voltage at 65 V. Free fatty acids were identified based on comparison to the theoretical reference standards in Lipid Annotator (Agilent) software with a mass deviation≤10 ppm and a total score≥60. Raw data were

processed using Profinder 10.0 (Agilent) for peak detection, alignment and integration. The matching tolerances were set as follows: mass tolerance, 20 ppm; retention time deviation tolerance, 0.3 min.

ICP-MS for Mg^{2+} concentration determination

Quadruple volume of nitric acid (Fisher Chemical) was added to the FATP2 protein (72.6 μM) following with overnight digestion. Then the solutions were diluted fifteen times with 1% nitric acid before subjected to MS detection. An inductively coupled plasma mass spectrometer (ICP-MS, Thermo Fisher ICAP RQ) was used for the determination of Mg^{2+} concentration in each sample with magnesium (Mg) standard solutions (Beijing General Research Institute of Nonferrous Metals) as control. The instrument was optimized daily before analysis to ensure optimal performance. The operating conditions were as follows: Plasma power 1550 W, cool gas flow 14 l/min, auxiliary gas flow 0.8 l/min, nebulizer gas flow 0.95 l/min. A series of Mg standard solutions with concentrations of 1, 2, 5, 10, 20, 50, and 100 μg/L were prepared from the stock solution (1 mg/ml) by diluting with 1% nitric acid aqueous solution. The calibration curve was constructed by measuring the signal intensities of these standard solutions. The samples were aspirated into the ICP-MS, and the Mg^{2+} concentration was determined based on the calibration curve. Qtegra ISDS software (integrated with instrument control tool) was applied for instrument operation and data analysis of the Thermo iCAP RQ ICP-MS system.

Mass spectrometry analysis of oleoyl-AMP, AMP and oleic acid

FATP2 samples with or without NaOH treatment were analyzed using an LC-MS system comprising an Agilent 1290 Infinity II UHPLC system tandem with Bruker Tims TOF Pro2 for abundance determination of oleoyl-AMP, AMP and oleic acid. For samples requiring NaOH treatment, final concentration of 0.5 M of NaOH was supplemented and the hydrolysis lasted for 30 minutes at 37 °C. The pH was adjusted to neutral with concentrated hydrochloric acid before centrifugation at 14,000g for 10 min (4 - 8 °C) and the supernatants were collected for the extraction of corresponding ligands.

For oleoyl-AMP and AMP extraction, 100 µl of each protein sample (29.3 µM) was supplemented with 400 µl pre-chilled (−80 °C) methanol to a final methanol concentration of 80% (v/v), following with 1-2h incubation at 4 °C. After centrifugation at 14,000g for 10 min the supernatants were collected. Chromatographic separation of oleoyl-AMP was achieved on an Intensity Solo2 C18 column (100 mm × 2.1 mm) with the mobile phase consisting of 0.1% (v/v) formic acid in water as solvent A and 0.1%(v/v) formic acid in ACN as solvent B. Chromatographic separation of AMP was achieved on an ACQUITY UPLC BEH Amide column (100 mm × 2.1 mm, 1.7 µm) with the mobile phase consisting of 15 mM ammonium acetate, 0.3% ammonium hydroxide in water as solvent A and 15 mM ammonium acetate, 0.3% ammonium hydroxide in 9:1 acetonitrile/water as solvent B. For oleic acid analysis, fatty acids were extracted as mentioned above in the section of 'LC–MS analysis of fatty acids contents'. The MS data were acquired using electrospray ionization in negative ion mode over 20-1300 m/z and 100-1350 m/z for oleoyl-AMP/AMP and oleic acid, respectively. TIMS-MS analysis was performed under the following conditions. The common MS source parameters were: end plate offset, 500 V; capillary voltage, 4500 V; nebulizer gas, 2 bar; drying gas, 8 L/min at 230 °C; and sheath gas, 4 L/min at 400 °C. The TIMS 1/k0 range was set to 0.10–1.50 V·s/cm² for oleoyl-AMP/AMP and 0.55–1.90 V·s/cm² for oleic acid. For both analytes, the ramp time and accumulation time were fixed at 100 ms. DataAnalysis (Bruker) was used for peak detection and integration.

Reconstitution of FATP2 into lipid peptidisc

For assay purpose, FATP2 variants were reconstituted into peptidiscs using the commercially synthesized NSPr peptide[25] during purification. Cell membrane was solubilized with 1% (w/v) DDM at 4 °C for 2 h. After high-speed centrifugation at 25,000 g for 1 h, the supernatant was loaded onto anti-FLAG resin. The column was washed with buffer containing 25 mM HEPES pH 7.4 and 150 mM NaCl and 0.03% (w/v) DDM. The target protein was assembled into the peptidisc on the anti-FLAG resin through incubation with buffer containing 25 mM HEPES pH 7.4, 150 mM NaCl and 1 mg/ml NSPr. Then the column was washed to remove free NSPr. The assembled FATP2 in peptidiscs were eluted and loaded onto a size-

exclusion column. The purified FATP2 peptidiscs complex was harvested for long chain acyl-CoA synthetase activity assay.

Acyl-CoA synthetase activity assay

Enzyme activity was measured by AMP production through HPLC (Dionex Ultimate 3000 UHPLC+) at wavelength of 259 nm. Reactions were performed in buffers containing 150 mM NaCl, 1 mM $MgCl_2$, 2.5 mg/mL cyclodextrin, with 200 μM CoA, 1 mM ATP, and 500 μM oleic acid, and 25 mM various choices of pH buffer. To examine the pH dependency, pH range was set between pH 4.0 and 9.0. For all other assay purposes, HEPES pH 7.4 was used. Reactions were terminated by the supplementation of chloroform. Additional chloroform extraction was performed to remove proteins and lipids. Each resulting aqueous sample was mixed with an equal volume of 5% perchloric acid and then run isocratically with a mobile phase (100 mM sodium acetate, 75 mM monosodium phosphate, pH 4.6) on a C18 column (Thermo fisher BDS Hypersil).

Preparation of liposomes and proteoliposomes

Air-dried POPC and POPG solution (POPC: POPG: C1-BODIPY-C12=164:487:1 molar ratio in chloroform) was resuspended to 20 mg/ml with buffer containing 25 mM HEPES pH 7.4, 150 mM NaCl. Protein-free liposomes were obtained by extrusion. Then 1% (w/v) β-OG (for N-FLAG-tagged WT FATP2a, 3G mutant, Y244W, H268A, E366A and K572A mutant) or 1.5% (w/v) DDM (for N-FLAG-GFP-tagged WT FATP2a and FATP2b) was supplemented for 30 min incubation before final 100 μg/ml FATP2 was added for another 2~3 h incubation at 4 °C. Detergents were removed by Bio-Beads SM2. Resulting proteoliposomes were harvested by ultracentrifugation at 75,500 g for 30 min, following with wash and ultracentrifugation for another four times to remove free C1-BODIPY-C12 and proteins. The pellets were resuspended with HEPES buffer at a final protein concentration of 0.25 mg/ml for FA transport assay.

FA transport assay

Each FA transport assay was performed by adding 25 µl proteoliposomes into 75 µl assay buffer containing 25 mM HEPES pH 7.4, 150 mM NaCl, 1 mM $MgCl_2$, 0.1% BSA (w/v, fatty acid and IgG free), 1 mM ATP and 0.2 mM CoA. After incubation for 2 min at 37 °C. The reaction was terminated with 900 µl ice-cold sodium acetate buffer (100 mM sodium acetate pH 4.5, 150 mM NaCl). After centrifugation at 75,500 g for 30 min at 4 °C, the supernatant was collected for measurement of the fluorescence intensity at excitation wavelength of 475 nm and emission wavelength of 516 nm.

AlphaFold-based structure prediction

AlphaFold-predicted structures of FATP1 (AlphaFold DB identifier: AF-Q6PCB7-F1), FATP3 (AlphaFold DB identifier: AF-Q5K4L6-F1), FATP4 (AlphaFold DB identifier: AF-Q6P1M0-F1), FATP5 (AlphaFold DB identifier: AF-Q9Y2P5-F1), FATP6 (AlphaFold DB identifier: AF-Q9Y2P4-F1) were downloaded from the UniProt database. Structural predictions of FATP2-inhibitor complexes were run using a local installed AlphaFold 3.0.2[42] on a high-performance computing cluster. We used the full-length FATP2 sequence as the protein input and modeled each candidate inhibitor, including lipofermata (CAS# 297180-15-5), grassofermata (CAS# 419547-11-8) and CB-6 (CAS# 240417-98-5), separately as a ligand input. The predictions were performed using the default AlphaFold3 inference settings. For each FATP2–ligand complex, the top-ranked model, ranked by the AlphaFold3 confidence score, was used for structural analysis.

Data availability

The atomic coordinates of WT FATP2 and K572 mutant generated in this study have been deposited in the Protein Data Bank (http://www.rcsb.org) with PDB ID 9VZP (https://doi.org/10.2210/pdb9vzp/pdb) and 20ZN (https://doi.org/10.2210/pdb20zn/pdb), and corresponding EM maps have been deposited in the Electron Microscopy Data Bank (https://www.ebi.ac.uk/pdbe/emdb/) with EMDB ID EMD-65482 (https://www.ebi.ac.uk/emdb/EMD-65482) and EMD-67436 (https://www.ebi.ac.uk/emdb/EMD-67436), respectively. The mass spectrometry raw data

have been deposited in MassIVE (http://massive.ucsd.edu/) with the dataset identifier MSV000102611 (http://doi.org/10.25345/C5125QQ5X). All other data are available in the manuscript or the supplementary information. Source Data are provided with this paper.

References

1 Houten, S. M., Violante, S., Ventura, F. V. & Wanders, R. J. The Biochemistry and Physiology of Mitochondrial Fatty Acid β-Oxidation and Its Genetic Disorders. *Annu Rev Physiol* **78**, 23-44, doi:10.1146/annurev-physiol-021115-105045 (2016).

2 Nohturfft, A. & Zhang, S. C. Coordination of lipid metabolism in membrane biogenesis. *Annu Rev Cell Dev Biol* **25**, 539-566, doi:10.1146/annurev.cellbio.24.110707.175344 (2009).

3 Zadoorian, A., Du, X. & Yang, H. Lipid droplet biogenesis and functions in health and disease. *Nat Rev Endocrinol* **19**, 443-459, doi:10.1038/s41574-023-00845-0 (2023).

4 Brennan, E., Kantharidis, P., Cooper, M. E. & Godson, C. Pro-resolving lipid mediators: regulators of inflammation, metabolism and kidney function. *Nat Rev Nephrol* **17**, 725-739, doi:10.1038/s41581-021-00454-y (2021).

5 Samovski, D., Jacome-Sosa, M. & Abumrad, N. A. Fatty Acid Transport and Signaling: Mechanisms and Physiological Implications. *Annu Rev Physiol* **85**, 317-337, doi:10.1146/annurev-physiol-032122-030352 (2023).

6 Spector, A. A. & Yorek, M. A. Membrane lipid composition and cellular function. *J Lipid Res* **26**, 1015-1035 (1985).

7 Grevengoed, T. J., Klett, E. L. & Coleman, R. A. Acyl-CoA metabolism and partitioning. *Annu Rev Nutr* **34**, 1-30, doi:10.1146/annurev-nutr-071813-105541 (2014).

8 Dutta-Roy, A. K. Cellular uptake of long-chain fatty acids: role of membrane-associated fatty-acid-binding/transport proteins. *Cell Mol Life Sci* **57**, 1360-1372, doi:10.1007/pl00000621 (2000).

9 Snaebjornsson, M. T., Janaki-Raman, S. & Schulze, A. Greasing the Wheels of the Cancer Machine: The Role of Lipid Metabolism in Cancer. *Cell Metab* **31**, 62-76, doi:10.1016/j.cmet.2019.11.010 (2020).

10 Kleinfeld, A. M., Chu, P. & Romero, C. Transport of long-chain native fatty acids across lipid bilayer membranes indicates that transbilayer flip-flop is rate limiting. *Biochemistry* **36**, 14146-14158, doi:10.1021/bi971440e (1997).

11 Hirsch, D., Stahl, A. & Lodish, H. F. A family of fatty acid transporters conserved from mycobacterium to man. *Proc Natl Acad Sci U S A* **95**, 8625-8629, doi:10.1073/pnas.95.15.8625 (1998).

12 Stahl, A. *et al.* Identification of the major intestinal fatty acid transport protein. *Mol Cell* **4**, 299-308, doi:10.1016/s1097-2765(00)80332-9 (1999).

13 Gimeno, R. E. *et al.* Targeted deletion of fatty acid transport protein-4 results in early embryonic lethality. *J Biol Chem* **278**, 49512-49516, doi:10.1074/jbc.M309759200 (2003).

14 Schaffer, J. E. & Lodish, H. F. Expression cloning and characterization of a novel adipocyte long chain fatty acid transport protein. *Cell* **79**, 427-436, doi:10.1016/0092-8674(94)90252-6 (1994).

15 Black, P. N., Ahowesso, C., Montefusco, D., Saini, N. & DiRusso, C. C. Fatty Acid Transport Proteins: Targeting FATP2 as a Gatekeeper Involved in the Transport of Exogenous Fatty Acids. *Medchemcomm* **7**, 612-622, doi:10.1039/c6md00043f (2016).

16 Melton, E. M., Cerny, R. L., DiRusso, C. C. & Black, P. N. Overexpression of human fatty acid transport protein 2/very long chain acyl-CoA synthetase 1 (FATP2/Acsvl1) reveals distinct patterns of trafficking of exogenous fatty acids. *Biochem Biophys Res Commun* **440**, 743-748, doi:10.1016/j.bbrc.2013.09.137 (2013).

17 Coe, N. R., Smith, A. J., Frohnert, B. I., Watkins, P. A. & Bernlohr, D. A. The fatty acid transport protein (FATP1) is a very long chain acyl-CoA synthetase. *J Biol Chem* **274**, 36300-36304, doi:10.1074/jbc.274.51.36300 (1999).

18 Falcon, A. *et al.* FATP2 is a hepatic fatty acid transporter and peroxisomal very long-chain acyl-CoA synthetase. *Am J Physiol Endocrinol Metab* **299**, E384-393, doi:10.1152/ajpendo.00226.2010 (2010).

19 Anderson, C. M. & Stahl, A. SLC27 fatty acid transport proteins. *Mol Aspects Med* **34**, 516-528, doi:10.1016/j.mam.2012.07.010 (2013).

20 Veglia, F. *et al.* Fatty acid transport protein 2 reprograms neutrophils in cancer. *Nature* **569**, 73-78, doi:10.1038/s41586-019-1118-2 (2019).

21 Glatz, J. F., Luiken, J. J. & Bonen, A. Membrane fatty acid transporters as regulators of lipid metabolism: implications for metabolic disease. *Physiol Rev* **90**, 367-417, doi:10.1152/physrev.00003.2009 (2010).

22 Hagberg, C. E. *et al.* Vascular endothelial growth factor B controls endothelial fatty acid uptake. *Nature* **464**, 917-921, doi:10.1038/nature08945 (2010).

23 Schulze, P. C., Drosatos, K. & Goldberg, I. J. Lipid Use and Misuse by the Heart. *Circ Res* **118**, 1736-1751, doi:10.1161/circresaha.116.306842 (2016).

24 Michos, E. D., McEvoy, J. W. & Blumenthal, R. S. Lipid Management for the Prevention of Atherosclerotic Cardiovascular Disease. *N Engl J Med* **381**, 1557-1567, doi:10.1056/NEJMra1806939 (2019).

25 Carlson, M. L. *et al.* The Peptidisc, a simple method for stabilizing membrane proteins in detergent-free solution. *Elife* **7**, doi:10.7554/eLife.34085 (2018).

26 Stahl, A., Evans, J. G., Pattel, S., Hirsch, D. & Lodish, H. F. Insulin causes fatty acid transport protein translocation and enhanced fatty acid uptake in adipocytes. *Dev Cell* **2**, 477-488, doi:10.1016/s1534-5807(02)00143-0 (2002).

27 Kolahi, K., Louey, S., Varlamov, O. & Thornburg, K. Real-Time Tracking of BODIPY-C12 Long-Chain Fatty Acid in Human Term Placenta Reveals Unique Lipid Dynamics in Cytotrophoblast Cells. *PLoS One* **11**, e0153522, doi:10.1371/journal.pone.0153522 (2016).

28 Watkins, P. A., Maiguel, D., Jia, Z. & Pevsner, J. Evidence for 26 distinct acyl-coenzyme A synthetase genes in the human genome. *J Lipid Res* **48**, 2736-2750, doi:10.1194/jlr.M700378-JLR200 (2007).

29 Stuhlsatz-Krouper, S. M., Bennett, N. E. & Schaffer, J. E. Substitution of alanine for serine 250 in the murine fatty acid transport protein inhibits long chain fatty acid transport. *J Biol Chem* **273**, 28642-28650, doi:10.1074/jbc.273.44.28642 (1998).

30 Stuhlsatz-Krouper, S. M., Bennett, N. E. & Schaffer, J. E. Molecular aspects of fatty acid transport: mutations in the IYTSGTTGXPK motif impair fatty acid transport protein function. *Prostaglandins Leukot Essent Fatty Acids* **60**, 285-289, doi:10.1016/s0952-3278(99)80001-5 (1999).

31 Kochan, G., Pilka, E. S., von Delft, F., Oppermann, U. & Yue, W. W. Structural snapshots for the conformation-dependent catalysis by human medium-chain acyl-coenzyme A synthetase ACSM2A. *J Mol Biol* **388**, 997-1008, doi:10.1016/j.jmb.2009.03.064 (2009).

32 Horswill, A. R. & Escalante-Semerena, J. C. Characterization of the propionyl-CoA synthetase (PrpE) enzyme of Salmonella enterica: residue Lys592 is required for propionyl-AMP synthesis. *Biochemistry* **41**, 2379-2387, doi:10.1021/bi015647q (2002).

33 Reger, A. S., Carney, J. M. & Gulick, A. M. Biochemical and crystallographic analysis of substrate binding and conformational changes in acetyl-CoA synthetase. *Biochemistry* **46**, 6536-6546, doi:10.1021/bi6026506 (2007).

34 Hisanaga, Y. *et al.* Structural basis of the substrate-specific two-step catalysis of long chain fatty acyl-CoA synthetase dimer. *J Biol Chem* **279**, 31717-31726, doi:10.1074/jbc.M400100200 (2004).

35 Kumar, M. *et al.* Definition of fatty acid transport protein-2 (FATP2) structure facilitates identification of small molecule inhibitors for the treatment of diabetic complications. *Int J Biol Macromol* **244**, 125328, doi:10.1016/j.ijbiomac.2023.125328 (2023).

36 Sandoval, A., Chokshi, A., Jesch, E. D., Black, P. N. & Dirusso, C. C. Identification and characterization of small compound inhibitors of human FATP2. *Biochem Pharmacol* **79**, 990-999, doi:10.1016/j.bcp.2009.11.008 (2010).

37 Ahowesso, C. *et al.* Chemical inhibition of fatty acid absorption and cellular uptake limits lipotoxic cell death. *Biochem Pharmacol* **98**, 167-181, doi:10.1016/j.bcp.2015.09.004 (2015).

38 Punjani, A., Rubinstein, J. L., Fleet, D. J. & Brubaker, M. A. cryoSPARC: algorithms for rapid unsupervised cryo-EM structure determination. *Nat Methods* **14**, 290-296, doi:10.1038/nmeth.4169 (2017).

39 Punjani, A., Zhang, H. & Fleet, D. J. Non-uniform refinement: adaptive regularization improves single-particle cryo-EM reconstruction. *Nat Methods* **17**, 1214-1221, doi:10.1038/s41592-020-00990-8 (2020).

40 Wang, N. *et al.* Structural basis of human monocarboxylate transporter 1 inhibition by anti-cancer drug candidates. *Cell* **184**, 370-383.e313, doi:10.1016/j.cell.2020.11.043 (2021).

41 Jumper, J. *et al.* Highly accurate protein structure prediction with AlphaFold. *Nature* **596**, 583-589, doi:10.1038/s41586-021-03819-2 (2021).

42 Abramson, J. *et al.* Accurate structure prediction of biomolecular interactions with AlphaFold 3. *Nature* **630**, 493-500, doi:10.1038/s41586-024-07487-w (2024).

43 Emsley, P. & Cowtan, K. Coot: model-building tools for molecular graphics. *Acta Crystallogr D Biol Crystallogr* **60**, 2126-2132, doi:10.1107/s0907444904019158 (2004).

44 Afonine, P. V. *et al.* Real-space refinement in PHENIX for cryo-EM and crystallography. *Acta Crystallogr D Struct Biol* **74**, 531-544, doi:10.1107/s2059798318006551 (2018).

45 Davis, I. W. *et al.* MolProbity: all-atom contacts and structure validation for proteins and nucleic acids. *Nucleic Acids Res* **35**, W375-383, doi:10.1093/nar/gkm216 (2007).

46 DeLano, W. L. *The PyMOL Molecular Graphics System.*, <http://www.pymol.org> (2002).

47 Pettersen, E. F. *et al.* UCSF Chimera--a visualization system for exploratory research and analysis. *J Comput Chem* **25**, 1605-1612, doi:10.1002/jcc.20084 (2004).

48 Pettersen, E. F. *et al.* UCSF ChimeraX: Structure visualization for researchers, educators, and developers. *Protein Sci* **30**, 70-82, doi:10.1002/pro.3943 (2021).

Acknowledgements

We would like to thank the following facilities at Westlake University: Cryo-EM Facility for providing cryo-EM support, High-Performance Computing Center for computational resources and related assistance, the Mass Spectrometry & Metabolomics Core Facility for ligands analysis, and Min Zhou and Dr. Yinjuan Chen from Instrumentation and Service Center for Molecular Sciences for the ICP-MS analysis.

Funding

This work was supported by the National Natural Science Foundation of China (Project No. 32571395), the State Key Laboratory of Gene Expression (Project No. 2025ZY01117), the Ministry of Science and Technology of China, National Key R&D Program (Project No. 2022YFA1303700), the Key R&D Program of Zhejiang (2024SSYS0036), the Zhejiang Key Laboratories Project (2024E10052) and Westlake Education Foundation.

Author Contributions

D.M. conceived the project and wrote the manuscript. D.M. supervised on and provided methodology to structural and functional studies. A.L. contributed to protein expression and purification, cryo-EM sample preparation, data collection, assay system set up and biochemical assays. J.S. contributed to cryo-EM data processing, model building, protein purification and related assays. X.X and S.F. performed mass spectrometry analysis. Y.Y. performed AlphaFold predictions of FATP2-inhibitor complexes.

Competing interests

The authors declare no competing interests.